Solar Adaptive Optics System Based on Software Control

Noriaki Miura [*], Takashi Kobayashi, Shinnosuke Sakuma, Susumu Kuwamura, Naoshi Baba [1], Yoichirou Hanaoka [2], Satoru Ueno [3], and Reizaburou Kitai [3]

Department of Computer Sciences, Kitami Institute of Technology, 165 Koen-cho, Kitami, Hokkaido 090-8507, Japan

[1] Department of Applied Physics, Graduate School of Engineering, Hokkaido University, Sapporo, Hokkaido 060-8628, Japan

[2] National Astronomical Observatory, 2-21-1 Osawa, Mitaka, Tokyo 181-8588, Japan

[3] Hida Observatory, School of Science, Kyoto University, Kamitakara, Takayama, Gifu 506-1314, Japan

[*] miura@cs.kitami-it.ac.jp

Abstract

An adaptive optics system for solar observations at the Hida Observatory is described, which is composed of commercially available low-cost devices and fully controlled with software in standard PCs. This AO system operates at a frame rate of more than 250 Hz by virtue of the image processing procedures used. From laboratory experiments, it was confirmed that this AO system was useful for the temporal wavefront-variation of less than 64 Hz. During solar observations at the Hida Observatory the AO system worked well, except for a few cases.

KEYWORDS: adaptive optics, solar observation

1. Introduction

Astronomical adaptive optics (AO) is a developing technology for real-time compensation of atmospheric turbulence [1)], and various AO systems are now working in many astronomical observatories. In Japan, the Subaru telescope has an AO system as one of observational equipments on the Cassegrain focus [2)]. The spread of AO in Japan, however, seems slow. This is because a total AO system is not commercially available, and must be individually designed for each observatory in consideration of various conditions, such as telescope optics, observational wavelength and seeing. On the other hand, devices for AO are becoming popular. Our purpose is to develop an AO system for solar observation using low-cost commercial devices.

The development of solar AO has been active since the early 1990s. Dunn described the solar AO system of the National Solar Observatory [3)]. In that system, a liquid-crystal wavefront sensor and a continuous face-plate adaptive mirror with 61 actuators were used. Acton and Smithson reported the Lockheed AO system [4)], which adopted a 19-segment adaptive mirror with piezoelectric actuators and a wavefront sensor with microlens arrays on an array of quad-cell detectors. Since then, many solar observatories have equipped AO systems. Moreover, scientific results have been reported from observations using an AO system [5)].

A recent approach to developing an AO system is the software-based control of a wavefront compensation process. Paterson *et al.* described their AO system, in which tasks were mainly processed with a digital signal processor [6)]. Keller et al. developed a PC-based AO system for infrared observations with the 1.5-m McMath-Pierce solar telescope [7)]. The major advantages of their approach are the exclusion of expensive hardware and the flexibility of the processing procedure. Therefore, we decided to develop a PC-based AO system that is

fully controlled by software. In addition, we designed our system to compensate for low-order turbulence in observations with the G-band (central wavelength of 430.6 nm).

To drive a PC-based system with enough speed, a simple and fast algorithm of image processing is necessary. As the observational wavelength is shorter, atmospheric conditions are usually worse, causing larger shifts of image positions on sensors. Thus, the image processing algorithm to be developed has to be useful in spite of large image shifts. We present an image processing procedure, which uses inversion, thresholding and centroid calculation.

In this paper, we describe details of our solar AO system. Its features are summarized as follows:

(a) It is equipped to the domeless solar telescope at the Hida Observatory in Japan,

(b) Commercially-available low-cost devices are used,

(c) It is fully controlled by software in PCs, and

(d) It is designed to compensate for low-order turbulence in rather short wavelength.

We first investigate the performance of our system in experiments in our laboratory, and then show the preliminary results of solar observations conducted at the Hida Observatory.

2. Outline of the System

Figure 1(a) illustrates our AO system. The incident light to the system is collimated with a lens, and then is reflected with a tip-tilt mirror and a deformable mirror. The tip-tilt mirror is used for the cancellation of the overall image-shift, while the deformable mirror corrects the wavefront disturbed by atmospheric turbulence. A part of the light reflected with these mirrors is split to an image-shift sensor and to a wavefront sensor. The compensated light is finally led to the imaging camera. Figure 1(b) shows the optical setup; Table 1 lists the devices used in

the system and their specifications.

2.1 Tip-tilt compensation

The image-shift sensor is just a high-speed CCD camera. Images taken with the camera are processed with a PC to obtain the image centroids. The image-shift vector is specified as the difference between the image centroid of a target frame and that of the first frame. The procedure of image processing is described in section 3.1. From the image-shift vectors, voltages applied to the mirror are determined.

The tip-tilt mirror is mounted on a piezo-driven tilting stage. The stage tilts horizontally and vertically according to voltages applied to two piezo-devices. We regarded the relation between the tilting amount and the applied voltage as linear and then experimentally measured the proportional coefficients.

In our system, the tip-tilt compensation works with about 300 Hz when the exposure time of the CCD camera is 3 ms. The field of view is 57.15”×57.15”, and is windowed to restrict the processing region as described later.

2.2 Wavefront compensation

The wavefront sensor is composed of a microlens array and a high-speed CCD camera. The aperture size of the microlens and the pitch between lenses are 0.48 mm and 0.5 mm, respectively. The focal length of the microlens is 19 mm. The 5×5 microlenses cover a CCD chip of 2.56×2.56 mm^2 in size. The diameter of the telescope aperture image on the microlens array is 2.5 mm, as shown in Fig. 2. We use twenty sub-apertures in the wavefront calculation. The field of view of each sub-aperture is 21.2”×21.2”, and the number of pixels per

sub-aperture is 50×50.

The deformable mirror has nineteen piezo-actuators. These actuators are arrayed in a honeycomb alignment and the separation between them is 2.4 mm. The continuous mirror surface is deformed by the actuators that push and pull the surface. The mirror has a clear aperture with diameter of 30mm. The diameter of the telescope aperture image on this mirror is designed to be 23.3 mm.

An image taken with the wavefront sensor is the array of solar sub-images. A small sunspot is taken into the field of view of the sub-images as a target. Using the procedure described in section 3.2, the shift vectors in the sub-images are detected and then converted to the tilts of the wavefront. From them, the voltages to be applied to the deformable mirror are derived with a matrix product.

We measured the amount of mirror deformation with an interferometer, changing applied voltages. Figure 3 plots the deformation of the mirror surface versus applied voltages. Linearity can be seen from this plot.

2.3 Image acquisition

An imaging camera captures solar images after the compensation of wavefront degraded by atmospheric turbulence. The image size is 512×512 (in a 2×2 binning mode) or 1024×1024 pixels, which corresponds to a 46”$\times$46” field of view. The image is taken with 18 (in a 2×2 binning mode) or 9 Hz. In the observational mode, the camera takes 50-100 images every 15 s. The image acquisition loop can continue as long as the hard disk space is not full.

2.4 System operation

All the PCs in our system are connected by a network, and each process in every PC can be controlled by a host PC. Its software system has a GUI interface, making it easy for users to operate the AO system.

3. Image Processing and Voltage Calculation

The main tasks in mirror-control PCs are to derive required information from images, calculate the control voltages and then apply the voltages to the mirrors. The important thing is to finish the entire procedure within the freezing time of the atmosphere. We have implemented a simple and fast procedure of image processing.

3.1 Image processing for tip-tilt compensation

Figure 4(a) is one of the images taken by the image-shift sensor. The target for measuring image shifts is the sunspot located in the left center. As can be seen, the size of the target is considerably smaller than the image field. Since the whole field is not needed for centroid calculation, we restrict the image field using a window function in order to save computational time. The window size and its position are specified by the user. Only inside the window are the pixel values inverted, and then thresholded to omit the background values. Figure 4(b) shows an image after processing. Finally, the image centroid is calculated inside the window. This image processing procedure will be useful for any atmospheric condition, because the processing speed does not depend on the amount of image shift. However, it requires a high-contrast target, such as a sunspot, for sensing.

3.2 Image processing for wavefront compensation

The procedure of the centroid calculation for a wavefront is similar to that in section 3.1, however, there are some additional procedures. First, a user must separate sub-apertures by setting a grid, because the centroid calculation should be done inside each sub-aperture. Figure 5(a) shows an image obtained with the wavefront sensor, on which a grid is superimposed. Another additional procedure is the compensation for brightness difference between sub-apertures. Such brightness difference is caused by the telescope aperture edges which fall on the sub-aperture field (see Fig. 2). To compensate the brightness difference, we use the so-called flat-field correction: we measure the variation of brightness on every sub-aperture field in advance, and calibrate pixel values using it [Fig. 5(b)]. Pixel inversion and thresholding follow, and Fig. 5(c) shows the image finally obtained. Centroid positions in sub-apertures are derived from this image.

Each centroid position is compared to its reference position to determine the shift vector. The shift vectors (Δx_k, Δy_k) (k=1,…, K) are related to the gradients of the wavefront phases at sub-apertures (x_k, y_k) as

$$\frac{2\pi}{\lambda f}\Delta x_k = \left.\frac{\partial \phi(x,y)}{\partial x}\right|_{(x_k,y_k)} \equiv A_k \qquad (1)$$

and

$$\frac{2\pi}{\lambda f}\Delta y_k = \left.\frac{\partial \phi(x,y)}{\partial y}\right|_{(x_k,y_k)} \equiv B_k \quad , \qquad (2)$$

where λ is the wavelength and f is the focal length of the microlens. Using them, we specify a column vector $\boldsymbol{g}$ with $2K$ elements of A_k and B_k (k=1,..., K).

3.3 Wavefront expansion

From a set of the wavefront gradients, we must derive the wavefront itself. As ordinarily done, we also adopt the Zernike polynomials to specify wavefront phases. We used first twenty Zernike terms except for the piston mode.

Using the Zernike polynomials, the wavefront phase is represented as

$$\phi(x,y) = \sum_{j=1}^{J} a_j Z_j(x,y) \quad , \tag{3}$$

where $Z_j(x, y)$ is the j-th term of Zernike polynomials in the orthogonal coordinates, a_j is its coefficient to be determined, and J is the number of polynomials. The set of coefficients a_j, being represented as a column vector $\boldsymbol{a}$, is calculated as [8,9)]

$$\boldsymbol{a} = \boldsymbol{\Psi}^{-1}\boldsymbol{g}, \tag{4}$$

where $\boldsymbol{\Psi}$ is a rectangular matrix with J columns and $2K$ rows, whose elements are partial derivatives of $Z_j(x, y)$ at each microlens position k, and $\boldsymbol{\Psi}^{-1}$ denotes the inverse.

3.4 Voltage calculation

We assume that the response of a piezo-actuator is linear and that all are identical. The displacement of the mirror surface at each piezo-actuator is, therefore, represented as

$$\Delta u_m = cV_m \quad , \tag{5}$$

where V_m is voltage applied to the m-th actuator (m=1,…, M) and c is a coefficient.

The relation of the displacement Δu_m to the wavefront is

$$\Delta u_m = \frac{\lambda}{2\pi}\phi(x_m, y_m) \quad . \tag{6}$$

Putting eq. (6) into eq. (5) and using the matrix form gives

$$\boldsymbol{V} = \boldsymbol{\Gamma a}\,, \tag{7}$$

where $\boldsymbol{V}$ is a column vector with m voltage values, and $\boldsymbol{\Gamma}$ is a rectangular matrix with J columns and M rows, whose elements are

$$G_{mj} = \frac{\lambda}{2\pi c} Z_j\left(x_m, y_m\right) \quad . \tag{8}$$

Putting eq. (4) into eq. (7), we finally obtain

$$\boldsymbol{V} = \boldsymbol{\Gamma \Psi}^{-1} \boldsymbol{g} \quad . \tag{9}$$

The matrix product $\boldsymbol{\Gamma \Psi}^{-1}$ can be calculated in advance, once the alignments of sub-apertures and piezo-actuators are set. That is, one matrix product of $\boldsymbol{\Gamma \Psi}^{-1}$ and $\boldsymbol{g}$, containing $2K \times M$ multiplications, gives the set of voltages to be applied to piezo-actuators.

4. Simulation Experiments

To investigate the performance of our AO system, we conducted experiments in our laboratory. We set a pseudo atmosphere-telescope system in front of the AO module. The light source was a He-Ne laser and a pinhole was used as an object. To simulate atmospheric turbulence, we introduced another deformable mirror that is a membrane type with 19 channels. We prepared two driving modes for the mirror: tip-tilt and turbulence. In the tip-tilt mode, the mirror surface remains flat but inclines with a given oscillation frequency. When the turbulence mode is selected, the mirror surface is corrugated with a given frequency. These frequencies can be tuned by a parameter in the software. In the following experiments, the AO system worked with 300 Hz for both tip-tilt and turbulence compensations.

4.1 Performance of tip-tilt compensation

We set the oscillation frequency in the tip-tilt mode to 32 Hz in the horizontal direction. Figure 6(a) shows the distribution of 200 image centroids without AO. As predicted, the centroids distributed horizontally. The deviations in horizontal and vertical directions were 3.26 and 0.35 pixels, respectively. On the other hand, the use of AO made the centroid distribution compact as shown in Fig. 6(b); the deviations became 0.68 and 0.31 pixels, respectively.

We repeated the same experiments changing the tip-tilt frequency. Table 2 lists the results of 32, 64, 128, and 254 Hz. As the driving frequency increased, the results became worse. When it was 128 Hz, the deviations were no longer improved. Moreover, the system became unstable at 254 Hz. We consider that our system effectively worked for inputs with the oscillation frequency of less than 64 Hz.

4.2 Performance of turbulence compensation

To evaluate the wavefront compensation, we sequentially calculated the normalized cross-correlation of every two neighboring frames. Such correlation values would be lowered by the temporal change of artificial turbulence introduced by the membrane mirror. When the AO system worked well, they would increase toward one.

Figures 7(a) and 7(b) show the temporal changes of the normalized correlation values without and with AO, respectively, when the turbulence frequency is 32 Hz; as can be seen, using AO considerably increased these values. Also, the average correlation values rose from 0.77 to 0.89. Table 3 lists the results in turbulence frequencies of 32, 64, 128, and 252 Hz. The tendency was similar to the tip-tilt experiments: compensation was effective up to 64 Hz,

while the results became worse for higher frequencies.

5. Application to Solar Observation

We attached our AO module onto the focal plane of the domeless solar telescope at the Hida Observatory, and conducted solar observations in September, 2005. The central wavelength was 430.6 nm and the bandwidth was 2 nm. We set the exposure times of both the image shift sensor and the wavefront sensor to 3 ms. As a result, the AO worked at about 250 Hz. Figure 8 shows the time sequences of frames observed without and with AO in the left and right columns, respectively. The observational date of these images is September 18. We used the twin-sunspot located in the upper left corner as a target for the centroid calculation. Comparing images in the right column to those in the left, we can see that the variation of the sunspot shape is suppressed. In this observation, we employed the first frame as a reference for wavefront calculation. Thus, good compensation would allow later frames to be identical to the first frame.

We repeated observations without and with the AO over a few days, Table 4 summarizes the observational results. The second column lists the state of the AO system. The third and fourth columns list the deviations of centroid positions in the horizontal and vertical directions, respectively. The deviations of centroid positions tended to be low when using AO. Figure 9(a) plots the centroid positions of 200 frames observed without AO at 7:41 on September 18 (JST). As shown in Fig. 9(b), which is the data observed at 8:02, the image shift was suppressed when the AO worked. However, the effect of the tip-tilt compensation differed from day to day. On September 21, the deviations were small in both horizontal and vertical directions, while, on September 23, they were notably larger in the horizontal direction. We infer that the effect of tip-tilt compensation depends on the wind velocity of the

upper air. It should be noted that there are usually several wind layers over a telescope [10].

Figures 10(a) and 10(b) plot the temporal changes of correlation values without and with AO, respectively. The data used are the same as in Fig. (9). As can be seen, the use of AO raised correlation values. The fifth column in Table IV lists the average cross-correlation values over 200 frames. When AO was used, the correlation values tended to be higher. However, there were results in which we could not confirm the effect of AO, for example, that at 7:41 September 23. We suspect that the temporal change of the atmospheric turbulence was too fast for our AO system to compensate it.

6. Discussion

It was necessary to estimate atmospheric conditions at the Hida observatory in designing AO. Kitai measured them with knife-edge tests and then reported that the spatial scale of turbulence was about 10 cm and it temporally changed by about 50 Hz [11]. In our wavefront sensor, wavefront slope was sampled at intervals of 12 cm. Although this interval is not short enough for full compensation, we consider that our wavefront sensor is available for measuring low-order turbulence. In the laboratory experiments, our AO system could partially compensate the temporal wavefront change up to 64 Hz. As a result, the upper limit of compensable frequency was larger than 50 Hz. In fact, we confirmed that images were improved with AO in the observations at the Hida Observatory. However, we sometimes felt that the processing speed was not enough for seeing conditions in our observations. Since seeing conditions change with various factors, such as site, season, date, time and wavelength, observations involved measuring them will be needed to clarify the effect of AO.

In this paper, we have not directly assessed the image quality, though we have shown correlation values between frames. To show the imaging quality through AO, the Strehl ratio

is frequently used in night-time observations, because there are many point-like objects available for use in the calculation of the Strehl ratio. On the other hand, unfortunately, it is difficult to obtain this for extended objects like the solar surface. We now are investigating how to evaluate the imaging performance of our AO system.

7. Summary

We described the details of our solar AO system, the main feature being its software-oriented nature. Thus, the process involved in the system is easily developed and improved. The major problem of a software-oriented system has been insufficient processing speed. To raise it, we have implemented a simple and fast procedure of image processing, and attained a driving frequency of more than 250 Hz. From experiments in our laboratory, we found that our AO system can partially compensate atmospheric turbulence of less than 64 Hz and the compensation became better for lower frequency. We confirmed the effect of wavefront compensation in most cases when applying the system to solar observations at the Hida Observatory. However, the conditions that assure successful compensation are not yet clear, and further investigation of the system's performance is needed in terms of atmospheric conditions.

Acknowledgements

We especially thank H. Mifune of Ricoh Co. for his help in making microlens arrays. This work was partially supported by both a Grant-in-Aid for Scientific Research (C) from Japan Society for the Promotion of Science (No. 17540209) and a foundation for university support from National Astronomical Observatory of Japan.

References

1. For example, *Adaptive Optics in Astronomy*, ed. F. Roddier (Cambridge University Press, Cambridge, 1999).
2. H. Takami, N. Takato, Y. Hayano, M. Iye, S. Oya, Y. Kamata, T. Kanzawa, Y. Minowa, M. Otsubo, K. Nakashima, W. Gaessler and D. Saint-Jacques: Publ. Astron. Soc. Jap. **56** (2004) 225.
3. R. B. Dunn: Proc. SPIE **1271** (1990) 216.
4. D. S. Acton and R. C. Smithson: Appl. Opt. **31** (1992) 3161.
5. G. B. Scharmer, B. V. Gudiksen, D. Kiselman, M. G. Löfdahl and L. H. M. Rouppe van der Voort: Nature **420** (2002) 151.
6. C. Paterson, I. Munro and J. C. Dainty: Opt. Express **6** (2000) 175.
7. C. U. Keller, C. Plymate and S. M. Ammons: Proc. SPIE **4853** (2003) 351.
8. W. H. Southwell: J. Opt. Soc. Am. **70** (1980) 998.
9. N. Roddier: Opt. Eng. **29** (1990) 1174.
10. H. Horikawa, N. Baba, M. Ohtsubo, Y. Norimoto, T. Nishimura and N. Miura: Appl. Opt. **43** (2004) 3097.
11. R. Kitai: Proc. Hida Observatory Users' Meeting, Kyoto Univ., Kyoto, 2004, p. 70 [in Japanese].

Figure captions

Figure 1. (a) Schematic illustration of the AO system. There are three units for wavefront compensation, tip-tilt compensation and observation, each of which is controlled by a respective PC. All the PCs are connected with the network and controlled with a host PC drawn in the upper right corner of the figure. (b) Photograph of the optical setup of the AO system.

Figure 2. A 5×5 microlens array is outlined by dotted circles. The telescope aperture edge and the occultation edge by the secondary mirror are shown by solid and dashed lines, respectively. These edges invade some sub-apertures of the microlens, causing variations of brightness in sub-aperture images.

Figure 3. The displacement of the mirror surface versus applied voltage. The dashed line shows the regression line.

Figure 4. Image processing for tip-tilt compensation: images (a) before and (b) after windowing, inverting, and thresholding procedures.

Figure 5. Image processing for wavefront compensation: (a) an observed image, (b) an image processed with flat-field correction, (c) an image after inverting and thresholding procedure. The white grid lines specify sub-fields for the centroid calculation.

Figure 6. Distributions of centroid positions (a) without and (b) with AO in the simulation experiments. The oscillation frequency of the membrane mirror was 32 Hz. The distribution

in (b) is compact by virtue of AO.

Figure 7 Cross-correlation values between two neighboring frames are plotted in the cases of (a) without and (b) with AO in the simulation experiments. The frequency of wavefront corrugation was 32 Hz. The correlation values in (b) are increased compared with (a).

Figure 8. Solar images observed without (left column) and with (right column) AO. These data set were observed at 7:41 and 8:02 on September 18, respectively. The top image is the first frame of the data set. The AO tries to keep the later images identical to the first frame. In the images in the right column, the shape change of the sunspot is suppressed.

Figure 9. Distributions of centroid positions; (a) without and (b) with AO in solar observations. Data set used here are the same as in Fig. 8. The use of AO makes the distribution compact.

Figure 10. Cross-correlation values between two neighboring frames are plotted in the cases of (a) without and (a) with AO in solar observations. Data set used here are the same as in Fig. 8. The correlation values in (b) tend to be larger than those in (a).

Table 1. Devices and their specifications.

Deformable mirror	Continuous facesheet, 19 piezo-actuators, hexagonal array, 30mm diameter
Tip-tilt mirror	Two-axis mount, 2 piezo-actuators
Microlens array	25 subapertures, 5x5 orthogonal array, 19 mm focal length
Sensing cameras	256×256 pixels, 10μm pixel size, 935 maximum frame rate
Imaging camera	1280×1024 pixels, 9 or 18 Hz frame rate (1×1 or 2×2 binning)
Tip-tilt control	Standard PC with Pentium IV 280 Hz
Wavefront control	Standard PC with Pentium IV 340 Hz

Table 2. Deviations of centroid positions.

Oscillation frequency (Hz)	Without AO		With AO	
	Horizontal (pixels)	Vertical (pixels)	Horizontal (pixels)	Vertical (pixels)
32	3.26	0.35	0.68	0.31
64	3.25	0.66	1.78	1.95
128	3.17	1.96	3.76	2.41
254	3.22	1.08	7.62	1.92

Table 3. Average of the normalized cross-correlation values between two neighboring frames.

Turbulence frequency (Hz)	Without AO	With AO
32	0.77	0.89
64	0.69	0.83
128	0.75	0.67
254	0.76	0.61

Table 4. Results of solar observations.

Date & Time (JST)	AO drive	Deviations of centroid positions (arcsec)		Average correlation value
		Horizontal	Vertical	
Sept. 18				
7:41	off	0.61	0.74	0.65
7:53	on	0.27	0.46	0.74
7:55	on	0.24	0.44	0.78
7:59	off	0.52	0.46	0.79
8:02	on	0.21	0.19	0.82
Sept. 21				
10:06	on	0.12	0.26	0.84
10:14	on	0.13	0.24	0.83
10:23	on	0.12	0.19	0.87
10:35	off	0.45	0.41	0.76
10:44	on	0.10	0.18	0.81
Sept. 23				
7:41	on	0.29	0.12	0.57
7:42	off	0.54	0.41	0.78
7:51	on	0.28	0.16	0.85
7:53	off	0.57	0.55	0.66
7:57	on	0.24	0.11	0.84
7:59	off	0.57	0.50	0.66

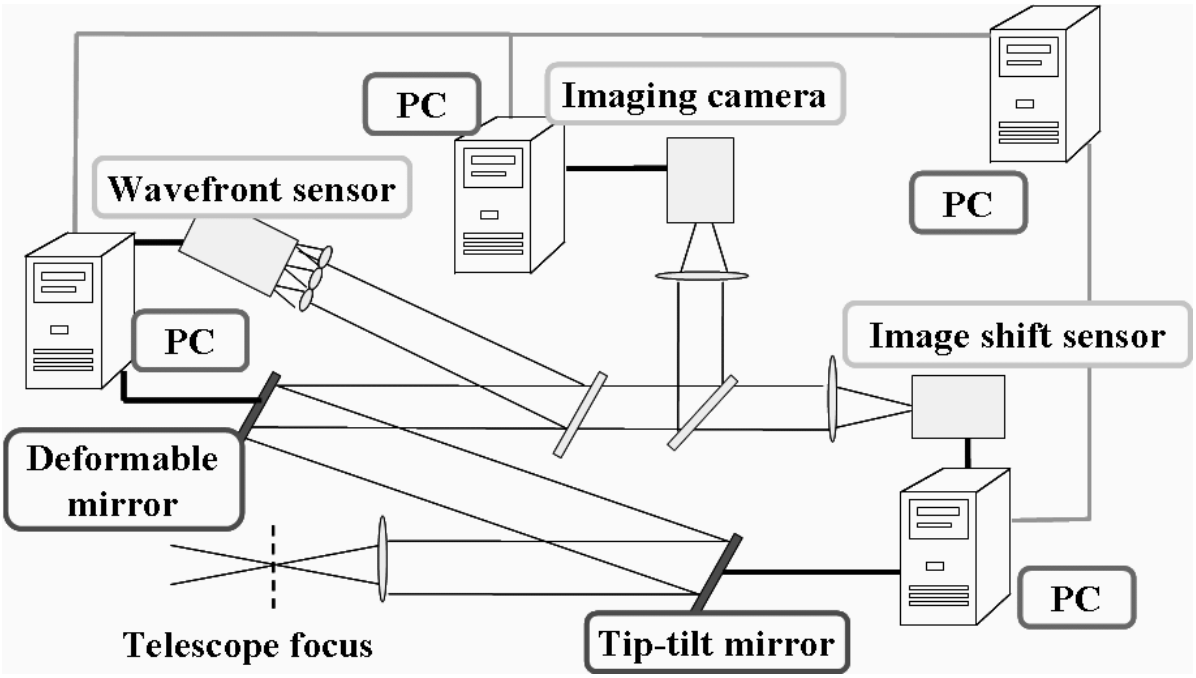

(a)

Fig. 1(a)

N. Miura et al.

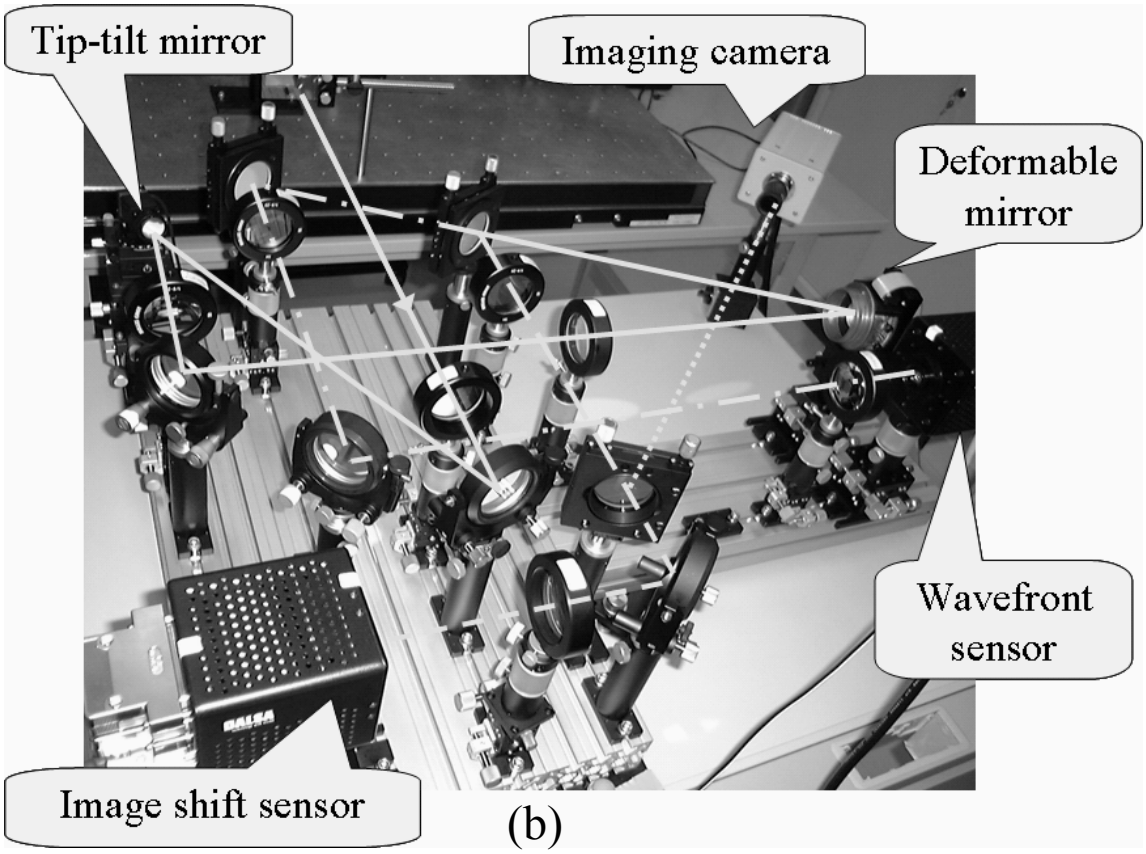

Fig. 1(b)

N. Miura et al.

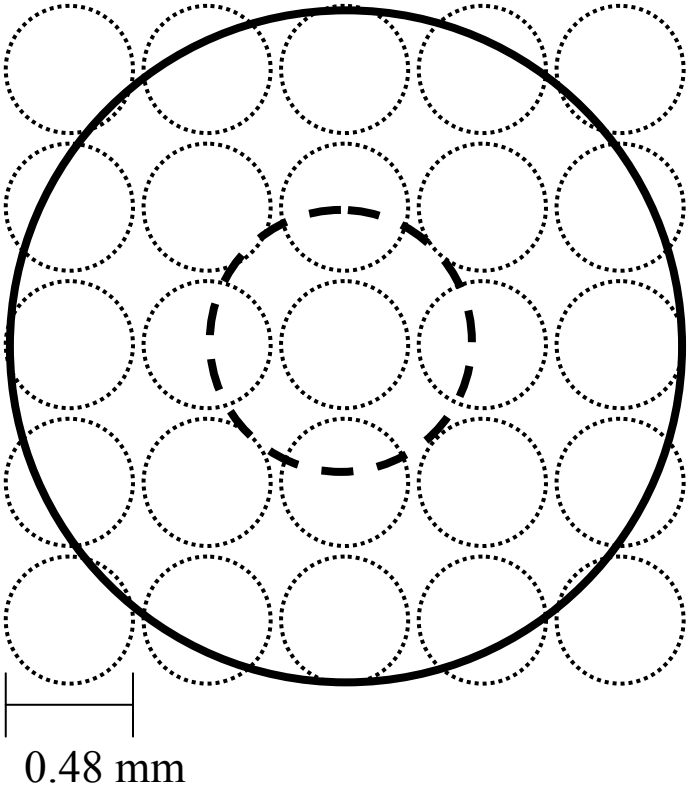

Fig. 2

N. Miura et al.

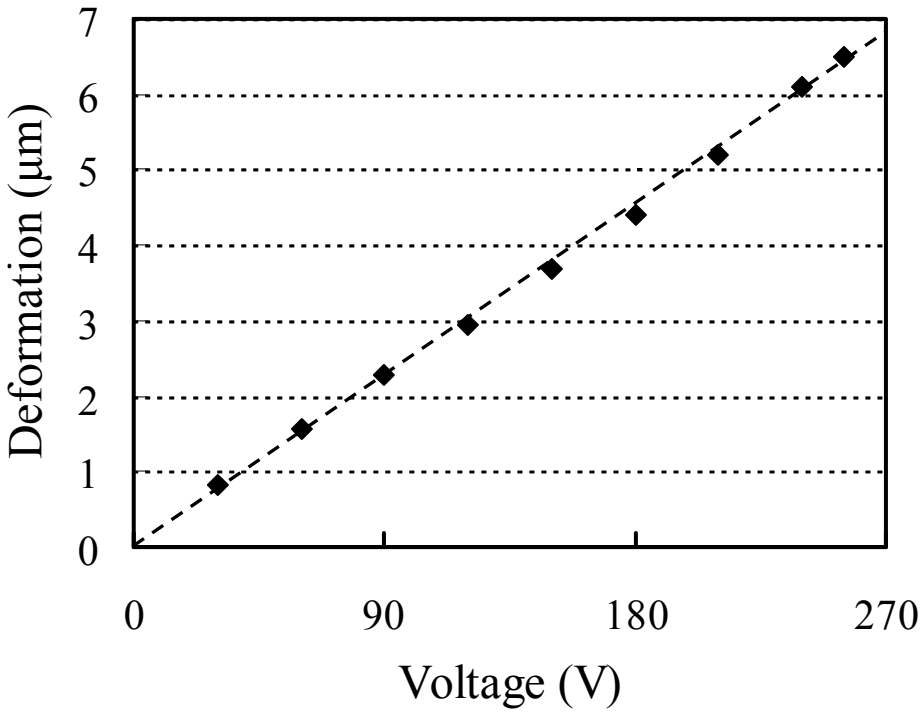

Fig. 3

N. Miura et al.

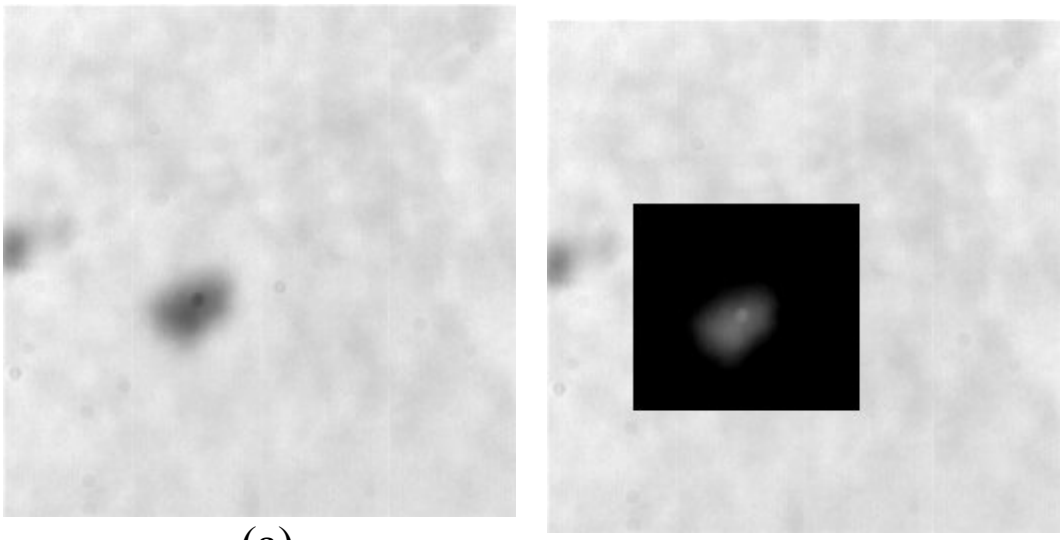

Fig. 4

N. Miura et al.

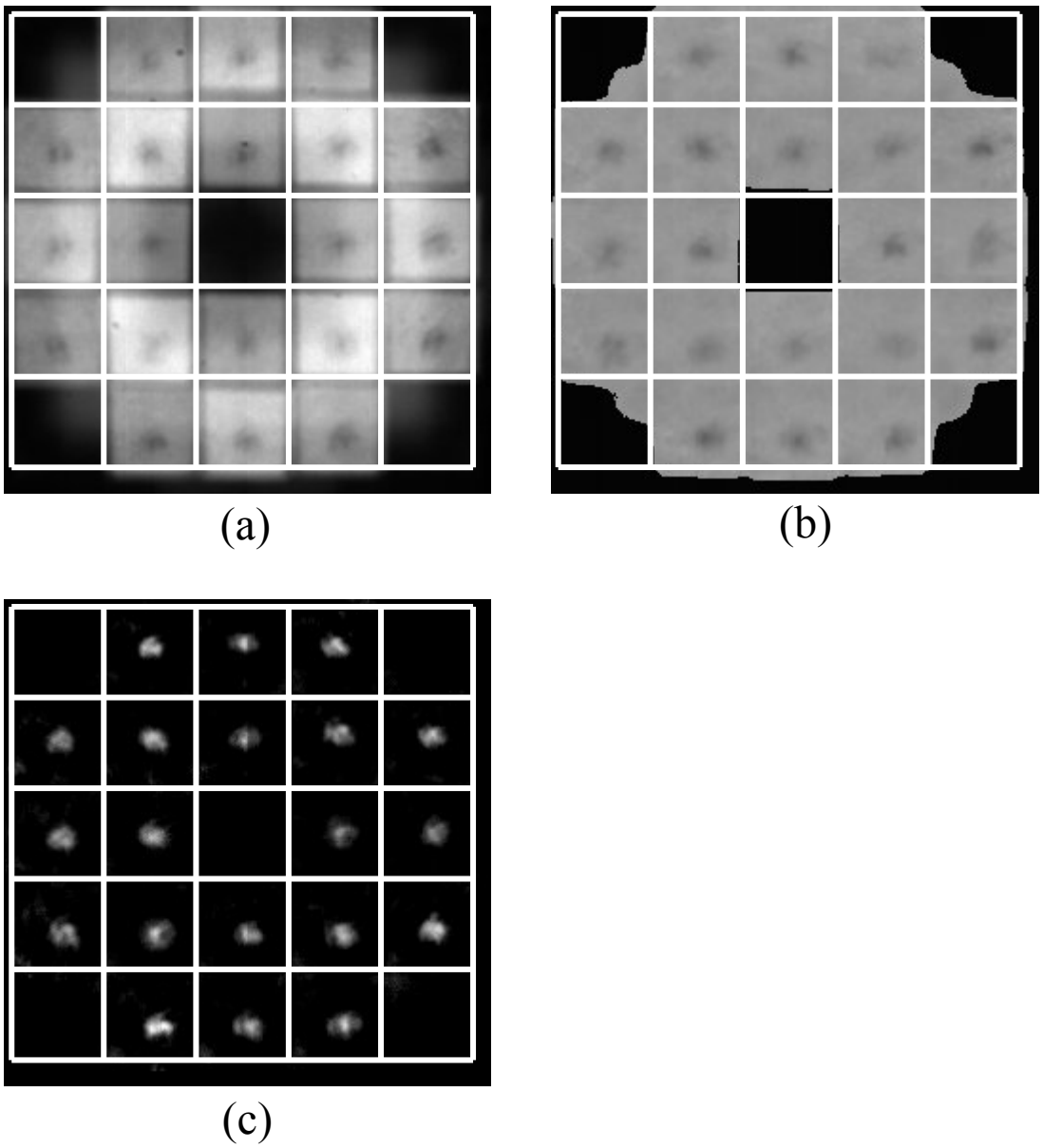

Fig. 5

N. Miura et al.

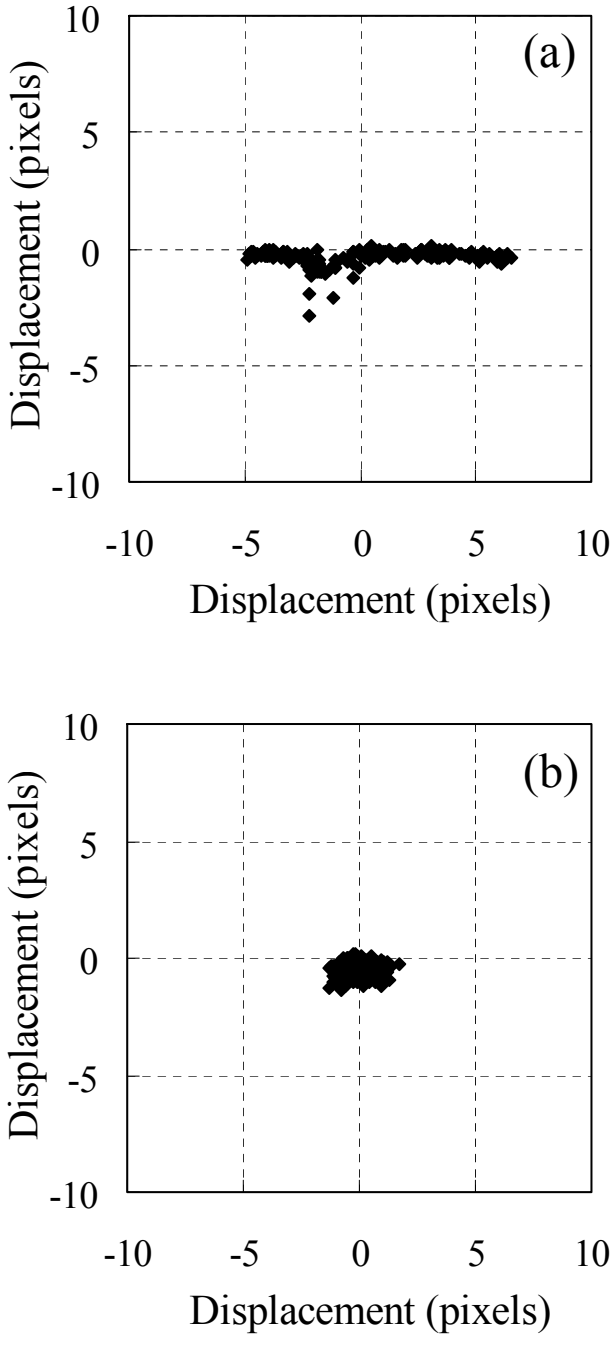

Fig. 6

N. Miura et al.

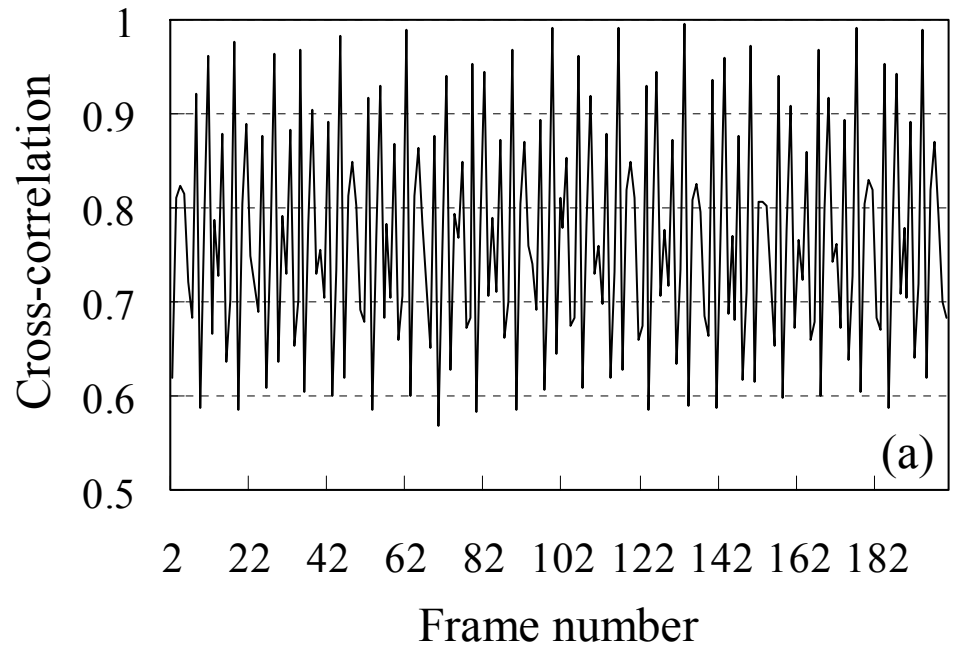

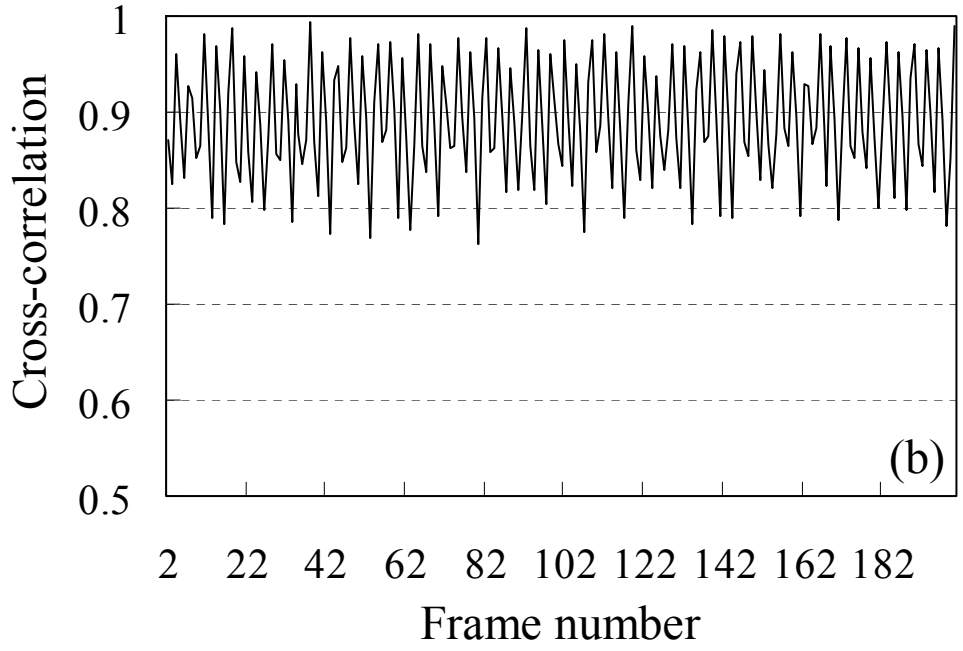

Fig. 7

N. Miura et al.

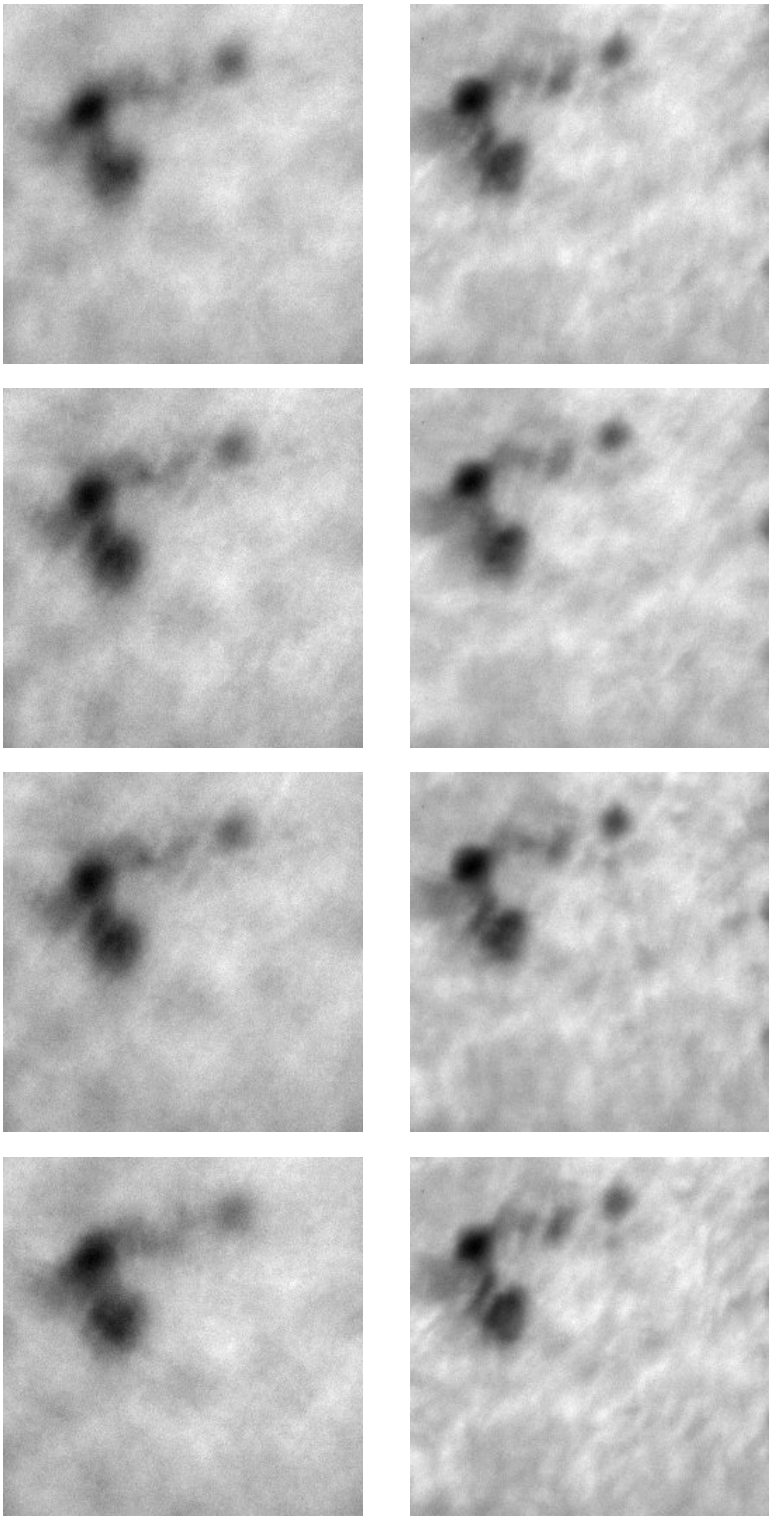

Fig. 8 N. Miura et al.

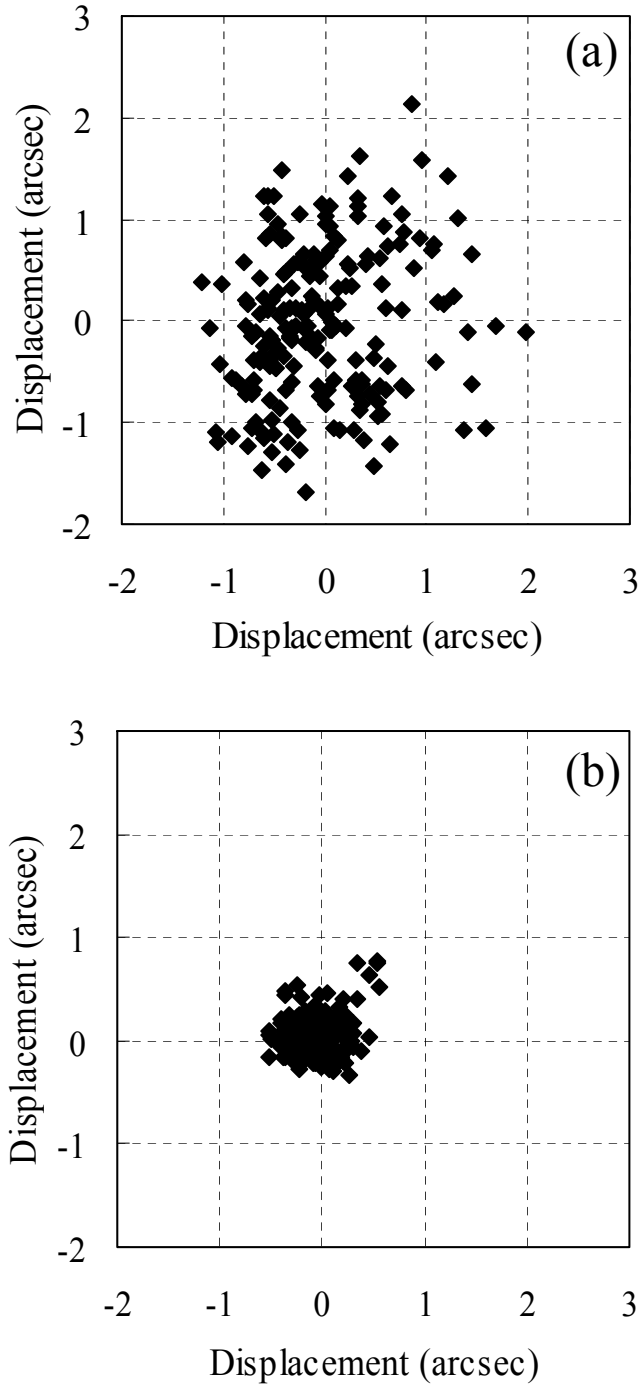

Fig. 9

N. Miura et al.

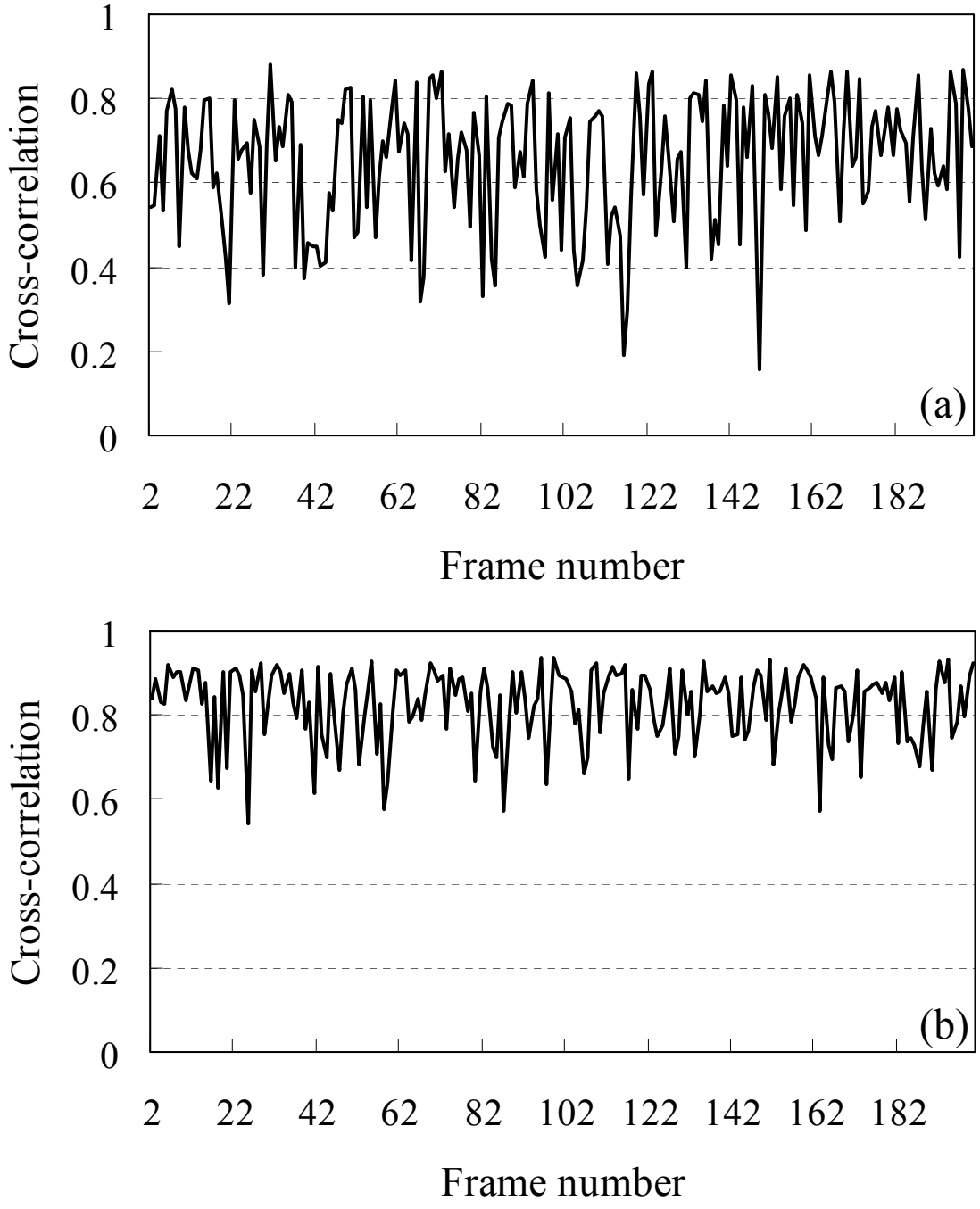

Fig. 10

N. Miura et al.